Applied-field magnetic structure and spectroscopy shifts of the effective spin-$\frac{1}{2}$ XY-like magnet Li$_2$CoCl$_4$

Zachary W. Riedel [1,2] Mykhaylo Ozerov [3,*] Stuart Calder [4] and Daniel P. Shoemaker [1,2,†]

[1]*Department of Materials Science and Engineering, University of Illinois Urbana-Champaign, Urbana, Illinois 61801, USA*
[2]*Materials Research Laboratory, University of Illinois Urbana-Champaign, Urbana, Illinois 61801, USA*
[3]*National High Magnetic Field Laboratory, Florida State University, Tallahassee, Florida 32310, USA*
[4]*Neutron Scattering Division, Oak Ridge National Laboratory, Oak Ridge, Tennessee 37831, USA*

Insulators containing chains of magnetic transition metal cations provide platforms for probing spin-$\frac{1}{2}$ dynamics and quantum critical behavior. Li$_2$CoCl$_4$ contains edge-sharing CoCl$_6$ octahedra that form chains along the crystallographic c axis and orders antiferromagnetically at zero field, but questions remain about its applied-field magnetic structure and the Co^{2+} spin state. Here, we show with neutron diffraction on a polycrystalline sample how the antialigned chains of cobalt moments begin to transition to a ferromagnetic state above 1.6 T. Further, using magnetic resonance absorption measurements and noninteracting spin models, we reveal the strongly anisotropic nature of the Co^{2+} ion's XY-like magnetic behavior ($g_\parallel = 2.77$ and $g_\perp = 5.23$) and its $J = \frac{1}{2}$ ground state. We therefore supply the magnetic structures and anisotropic description needed to explore the dynamics of the field-driven magnetic phases, laying the foundation for further experimental and theoretical studies.

I. INTRODUCTION

Low-dimensional magnetic materials frequently provide access to quantum behavior, and scattering studies on unexplored, spin-$\frac{1}{2}$ materials are critical for validating low-dimensional magnetism models that may be extended to higher-dimensional systems [1]. Of note here, several compounds with chains of edge-sharing Co$^{2+}X_6$ polyhedra have exhibited quantum criticality [2–4]. We identified Li$_2$CoCl$_4$ as a low-dimensional magnetism candidate with a dimensional analysis toolkit [5]. Li$_2$CoCl$_4$ contains Co^{2+} octahedrally coordinated to Cl$^-$, forming edge-sharing polyhedral chains along the crystallographic c axis.

The ionic conductivity of Li$_2M$Cl$_4$ compounds has been studied extensively [6–15], but magnetic property measurements have been limited to susceptibility data used to determine the spin states of Mn^{2+} and Fe^{2+} in cubic Li$_2$MnCl$_4$ [16] and Li$_2$FeCl$_4$ [17]. For orthorhombic Li$_2$CoCl$_4$, high temperature susceptibility data indicate spin-$\frac{3}{2}$ (high-spin) behavior with significant unquenched orbital angular momentum, and heat capacity data point to a ground-state Kramers doublet ($J = \frac{1}{2}$) dominating low-temperature behavior [18]. Other high-spin Co^{2+} chlorides exhibit similar effective spin-$\frac{1}{2}$ behavior, leading to fruitful studies of spin excitations and quantum criticality [3,19–22]. Therefore, we were encouraged to map the magnetic phases of Li$_2$CoCl$_4$.

At zero field, Li$_2$CoCl$_4$ orders antiferromagnetically with P_Cbam magnetic space group symmetry. The Co^{2+} magnetic moments align within edge-sharing CoCl$_6$ chains and antialign between nearest-neighbor chains. The magnetic

susceptibility and heat capacity shift with increasing field, leading to three proposed magnetic phase regions separated by transitions near 1.6 T and 3.5 T at 2 K [18]. The magnetic structures of the applied-field regions are unknown. The low-field region is antiferromagnetic, likely similar to the zero-field magnetic ordering. The intermediate-field region may be ferrimagnetic, with chain rotations reminiscent of the structurally similar compound CoCl$_2 \cdot$ 2H$_2$O [23,24], though the data are also consistent with a spin-flop reorientation. Finally, in the high-field region, not sharply delineated from the intermediate-field one, the Li$_2$CoCl$_4$ moment chains are likely aligned, but with no well-defined Curie temperature in the magnetic susceptibility.

Here, we use polycrystalline Li$_2$CoCl$_4$ to probe the applied-field regions' magnetic structures with neutron diffraction, particularly that of the previously ambiguous intermediate-field region. Additionally, we extract several parameters from applied-field infrared spectroscopy data, such as the spectroscopic g factors, to discuss the role of spin-orbit coupling (SOC) and octahedral distortion on the magnetic properties of Li$_2$CoCl$_4$.

II. MATERIALS AND METHODS

We prepared polycrystalline Li$_2$CoCl$_4$ as previously described [18]. We ground LiCl (99.9%, Alfa Aesar) and CoCl$_2$ (99.7%, Alfa Aesar) under argon, sealed the mixture under vacuum, heated it to 550 °C at 10 °C/min, held for 12 h, then cooled to room temperature at 10 °C/min. We ensured that the highly hygroscopic LiCl and Li$_2$CoCl$_4$ powders remained under inert atmospheres during synthesis and characterization.

We collected neutron diffraction data on the HB-2A beamline at the High Flux Isotope Reactor at Oak Ridge National Laboratory (ORNL). To avoid grain reorientation

*Contact author: ozerov@magnet.fsu.edu
†Contact author: dpshoema@illinois.edu

under applied field, we pressed pellets of Li_2CoCl_4 for the diffraction experiment. Under argon, we pressed 1.5 g of powder into around 30 1/8" diameter pellets. We then sealed the pellets under vacuum, transported them to ORNL, and loaded them under helium into a 6 mm diameter vanadium canister. The top of the canister was packed with aluminum foil before being hermetically sealed.

We collected constant wavelength (2.41 Å) neutron diffraction data using a Ge(113) monochromator with the instrument in an open-open-12' premono, presample, predetector collimation. The sample was cooled to base temperature (1.5–1.6 K) under zero field before collecting powder scans that covered 2θ angles from 6.025° to 127.525° in 0.05° steps with $\mu_0H = 0$, 0.8, 1.5, 2.5, 3.5, 4.5, and 5.5 T. We also collected a zero-field scan at 20 K (above the ordering temperature). The cryomagnet contributed a significant reflection at $2\theta = 19.9°$. Sweeping scans monitored select magnetic reflections with increasing field or temperature, also after zero-field cooling. To analyze the neutron diffraction data, we used GSAS-II [25] in combination with the Bilbao Crystallographic Server's K-SUBGROUPSMAG program [26], generating magnetic structure images with VESTA [27].

We performed magnetoinfrared measurements at the infrared (IR) spectroscopy facility at the National High Magnetic Field Laboratory with a 17.5 T vertical-bore superconducting magnet coupled to a Bruker Vertex 80v FTIR spectrometer. In an argon glovebox, a 3–5 mg polycrystalline sample was bonded with n-eicosane and loaded between two polypropylene layers to protect it from oxygen and moisture. We placed the sample in a Voigt geometry so the incoming IR light was perpendicular to the magnetic field. A composite Si bolometer (IR Labs) collected the transmitted IR light with a spectral range of 10–1100 cm^{-1} (0.3–33 THz) and a resolution of 0.3 cm^{-1} (9 GHz). Additionally, we placed a low-pass THz filter (QMC Instruments) with a 120 cm^{-1} cutoff frequency in front of the sample to increase sensitivity in the far-IR (FIR) range and to minimize radiative heating. IR data were collected near 5 K.

The FIR transmission spectra were divided by a reference spectrum constructed from the maximum transmission at each wave number across all spectra measured at different magnetic fields. Such normalized transmission spectra, T_B, are only sensitive to intensity changes induced by the magnetic field and eliminate contributions from magnetic-field-independent vibrational absorption and instrument artifacts. The magnetic resonance absorption spectrum is then calculated as $A = -\log_{10}(T_B)$, and results were analyzed using the EPR analysis package EASYSPIN [28].

III. RESULTS AND DISCUSSION

A. Zero- and low-field magnetic structures

We first confirmed that the zero-field magnetic structure matches that determined previously. The data refines well to the antiferromagnetic structure with P_Cbam (BNS No. 55.363) magnetic space group symmetry (see Supplemental Material [29]). For the magnetic space group P_Cbam, only reflections where $h + k \neq 2n$ are allowed, whereas the nuclear $Cmmm$ space group only allows reflections where $h + k = 2n$,
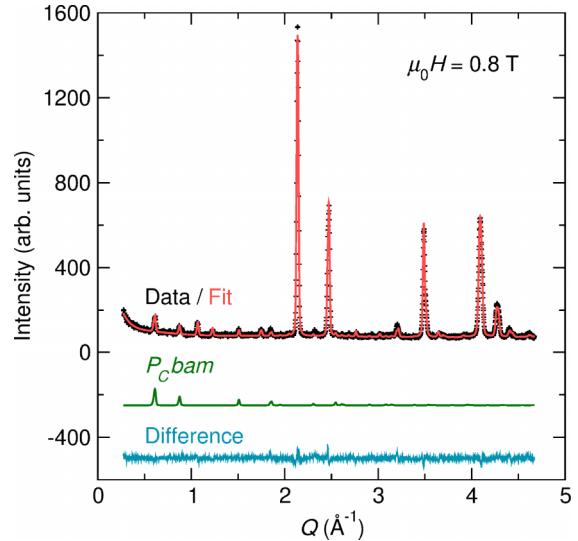

FIG. 1. The neutron powder diffraction data collected at 1.5 K and 0.8 T refine well to the antiferromagnetic phase also observed at zero field with a 2.02(3) μ_B moment along the c axis for Co^{2+}. The refined lattice parameters are $a = 7.1711(3)$, $b = 10.2393(5)$, and $c = 3.6111(2)$ Å.

making it simple to identify the magnetic ordering reflections. The magnetic structure is commensurate, with the propagation vector $\mathbf{k} = (1,0,0)$. The magnetic moments are aligned within the Co^{2+} chains and antialigned between nearest-neighboring chains along the nuclear cell's ab-plane diagonal. The antiferromagnetic interchain interactions lead to the previously reported cusp in the magnetic susceptibility and the negative Curie-Weiss temperature [18]. The refined moment is 2.10(3) μ_B. Though the moment in this study is slightly lower than the previously refined value 2.19(4) μ_B, the refinement standard errors are likely underestimated. Since we were able to produce a closer fit to peak intensities in this work, especially nuclear intensity, we will use 2.10 μ_B here. The 20 K, zero-field data in the paramagnetic region is included in the Supplemental Material for comparison [29].

We noticed several low-intensity impurity peaks at $2\theta = 17.0$, 30.4, 46.6, 53.0, and 68.5° ($Q = 0.77$, 1.37, 2.06, 2.32, and 2.93 Å^{-1}), the largest impurity peak being only 0.8% the intensity of the largest Li_2CoCl_4 peak. The $Q = 0.77$ Å^{-1} peak also appears in x-ray diffraction data after exposing a sample to air for 15–30 s before sealing it under vacuum [29]. The reflections do not change with temperature, indicating they are nonmagnetic, and they do not influence data analysis.

Prior magnetic susceptibility and heat capacity data indicate that the low-field magnetic structure (<1.6 T) matches the zero-field structure. At 0.8 T, we observe the same magnetic reflections as in the zero-field case, associated with a loss of C centering, but with slightly decreased intensity. Refinements give an unconstrained magnetic moment of 2.02(3) μ_B (Fig. 1), indicating some magnetic intensity may become paramagnetic background, though restricting the moment to 2.10 μ_B gives a nearly identical fit. With the field increased to 1.5 T, just below the 1.6 T transition to the intermediate-field phase, we can again refine the data well to the P_Cbam structure with a constrained 2.10 μ_B moment or a refined moment of
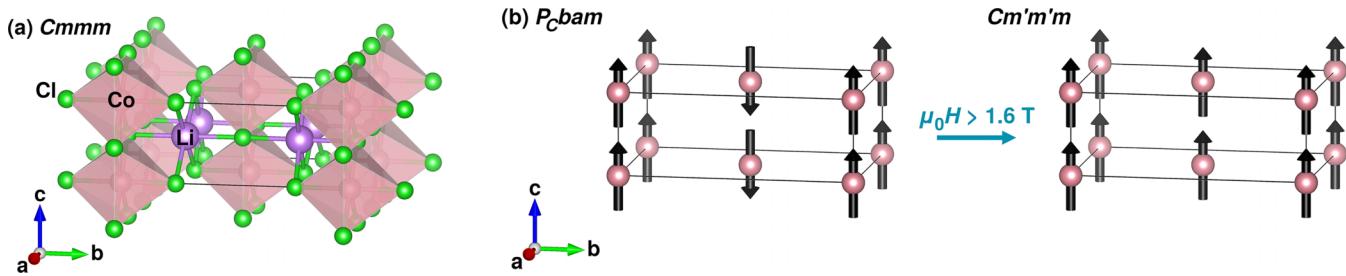
FIG. 2. The nuclear and magnetic cells of Li_2CoCl_4 are identified by their space groups. (a) The nuclear (and paramagnetic) unit cell contains chains of edge-sharing Co–Cl octahedra along c connected by chains of Li–Cl octahedra along a. (b) At zero field and below ~7 K, Co^{2+} chains are ferromagnetic with antiferromagnetic interchain interactions, breaking the cell's C centering. For applied fields above 1.5–1.6 T, ferromagnetic ordering emerges as the antiferromagnetic interactions are overcome.

1.96(3) μ_B. See the Supplemental Material [29] for the 1.5 T refinement.

B. Field-induced moment rotation

Between the 1.5 T and 2.5 T scans, the $h + k \neq 2n$ antiferromagnetic structure reflections, e.g., (010), (100), and (120), lose significant intensity while the $h + k = 2n$ reflections allowed by the C-centered nuclear cell, e.g., (110) and (020), gain intensity. The intensity shifts indicate a spin reorientation to a $\mathbf{k} = \mathbf{0}$ magnetic structure. Because of the nuclear cell's C centering, only ferromagnetic arrangements are consistent with $\mathbf{k} = \mathbf{0}$ ordering. Unlike for $CoCl_2 \cdot 2H_2O$ [23,24], we do not observe new peaks associated with a ferrimagnetic phase where one-third of the chains are antialigned. The difference in behavior may be due to the distance between antialigned chains in the zero-field structures (5.6 Å for $CoCl_2 \cdot 2H_2O$ and 6.2 Å for Li_2CoCl_4), producing a weaker next-nearest-neighbor (antiferromagnetic) exchange interaction in Li_2CoCl_4, and thus a lower barrier to overcoming the interaction with applied field. Instead, in Li_2CoCl_4 a spin reorientation begins to align the chains of Co^{2+} magnetic moments. The exact nature of the moment reorientation cannot be determined. If the reorientation involves a spin flop, as previously proposed, a magnetic field applied along the c axis would lead to a temporary flop to a hard axis perpendicular to c before a strong enough field produced a ferromagnetic arrangement of moments along c. Since the magnetic field is not applied along a specific crystallographic direction, we cannot confirm nor repudiate the presence of a spin-flop phase.

The randomly oriented structural grains lead to a slow evolution of the magnetic diffraction intensity with increasing field and a mixture of magnetic phases. For some of the randomly oriented structural grains in the sample, the magnetic field will align with the crystallographic axis preferred by the magnetic anisotropy, leading to the lowest-energy ferromagnetic arrangement and coherent magnetic scattering intensity. In contrast, for grains where the magnetic field is not aligned with the anisotropy-preferred direction, the competing perturbations will lead to moment canting off the anisotropy-preferred axis toward the field, explaining the previously observed net magnetization for a polycrystalline sample [18]. The magnetic scattering reflects the random distribution of these grains with canted moments and thus their randomly distributed moment orientations.

Several ferromagnetic models can successfully capture the additional magnetic intensity at high fields. The simplest model uses the maximal magnetic space group $Cm'm'm$ (BNS No. 65.485), which constrains the cobalt magnetic moments along the crystallographic c axis. Additional maximal magnetic groups are considered in the Supplemental Material [29]. Figure 2 shows the P_Cbam and $Cm'm'm$ magnetic unit cells along with the nuclear cell. Considering lower-symmetry, commensurate magnetic structures with canted moments does not improve fits to the ferromagnetic intensity. For example, the $C2'/m'$ space group symmetry (BNS No. 12.62) is the highest symmetry $\mathbf{k} = \mathbf{0}$ magnetic space group possible for Li_2CoCl_4 that allows for moment components along a and c. Refinements to the 5.5 T data using $C2'/m'$ ($M_a = 1.5(2)\,\mu_B$, $M_c = 1.7(1)\,\mu_B$, $|M| = 2.3(1)\,\mu_B$) gave a similar fit to the simpler $Cm'm'm$ model [29]. Likewise, an arrangement with $P\bar{1}$ magnetic symmetry (BNS No. 2.4) allows for moment components along all three crystallographic directions and gives a similar fit ($|M| = 2.3(2)\,\mu_B$). While there is ambiguity in the refinements regarding the $Cm'm'm$, $C2'/m'$, and $P\bar{1}$ magnetic symmetries, the $P\bar{1}$ scenario is likely more consistent with the polycrystalline sample's evolution due to the previously discussed randomness of the structural grains' orientations relative to the applied magnetic field, leading to an average magnetic structure with moment components along all three crystallographic directions.

The best refinement models above 1.6 T involve both the antiferromagnetic P_Cbam magnetic phase and a ferromagnetic $\mathbf{k} = \mathbf{0}$ structure. Using the simplest model ($Cm'm'm$ symmetry) allows us to track the evolution of the magnetic structure of Li_2CoCl_4 at magnetic fields greater than 1.6 T by refining the data with contributions from the P_Cbam antiferromagnetic structure and the $Cm'm'm$ ferromagnetic structure. The moment is constrained to be equal in the two magnetic phases when both are refined. The full Q range refinements for the 2.5, 3.5, 4.5, and 5.5 T data are shown in Fig. S4 [29]. Table I contains the refined phase fractions of the P_Cbam and $Cm'm'm$ magnetic structures and the refined cobalt magnetic moment for each magnetic field.

To highlight the changing magnetic contributions with increasing field, Fig. 3 compares the 0.8, 2.5, and 5.5 T refinements, corresponding to the previously described low-, intermediate-, and high-field regions. Since the intermediate-field region involves the greatest competition between the antiferromagnetic and ferromagnetic interactions, the refined

TABLE I. Rietveld refinement results for base-temperature, constant-applied-field scans are listed. Scans below 1.6 T only include the antiferromagnetic $P_C bam$ phase, while those above 1.6 T also include the ferromagnetic $Cm'm'm$ phase. The Co^{2+} magnetic moment is along the c axis in both cases.

Field (T)	Magnetic phase (% $P_C bam$–% $Cm'm'm$)	Refined moment (μ_B)
0	100–0	2.10(3)
0.8	100–0	2.02(3)
1.5	100–0	1.96(3)
2.5	81(6)–19(6)	1.59(7)
3.5	42(3)–58(3)	1.76(6)
4.5	17(2)–83(2)	2.07(6)
5.5	10(2)–90(2)	2.05(6)

magnetic moment is significantly reduced for the 2.5 and 3.5 T data. Likewise, while most of the refinements are qualitatively identical if the cobalt magnetic moment is constrained to the zero-field value of $2.10\,\mu_B$, the 2.5 and 3.5 T refinements significantly change (Fig. S5 [29]). At higher fields where the ferromagnetic phase dominates, the refined moment returns, within error, to its zero-field value, and constraining the moment to $2.10\,\mu_B$ does not influence the fit.

The emergence of the ferromagnetic phase with increasing field can be monitored more closely by tracking the relatively high intensity (010) reflection associated with the antiferromagnetic phase (Fig. 4). Above 1.6 T, the (010) intensity drops until the intensity levels off near 4.5 T. The drop in (010) reflection intensity at 1.6 T matches the slope change of the magnetization curve, the susceptibility's leveling off below the critical temperature, and the emergence of a hump in the magnetic heat capacity alongside a sharper peak [18]. The suppression of the heat capacity peak along with the
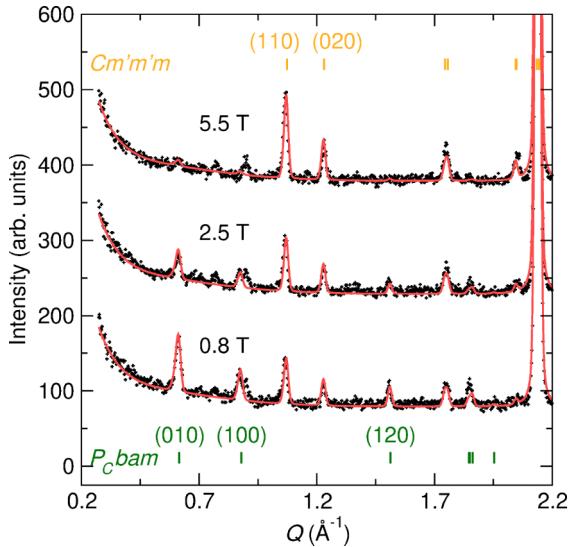

FIG. 3. Neutron powder diffraction data from the three regions (antiferromagnetic, spin-reorientation, ferromagnetic) are shown with several reflections labeled to highlight the phase contribution changes with increasing field. All unfit peaks are from the instrument/impurity features mentioned in the main text.
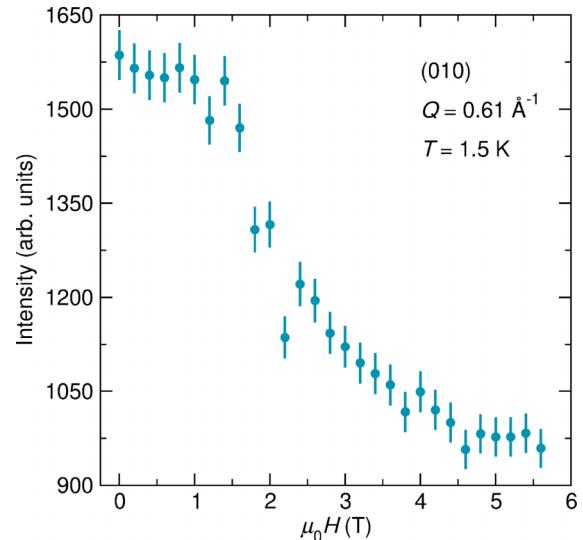

FIG. 4. With increasing field, the antiferromagnetic (010) reflection intensity is constant before decreasing with the emergence of the ferromagnetic phase near 1.5–1.6 T. Above 4.5 T, the intensity levels off as the ferromagnetic phase dominates.

emergence of a hump, therefore, is due to the reduction of antiferromagnetic regions and the short-range aligning of chains in newly formed ferromagnetic regions of the randomly oriented polycrystalline sample. While tracking the (010) reflection, we also captured changes in lower intensity reflections with the other diffractometer detectors: the antiferromagnetic (100) reflection and the nuclear/ferromagnetic (131) reflection. Both show the same trend of increasing ferromagnetic intensity and decreasing antiferromagnetic intensity above 1.5–1.6 T [29].

By the time the field reaches 5.5 T, the (010) reflection intensity has approached the experimental background, the majority of the sample is no longer antiferromagnetic, and the magnetic anisotropy likely favors an arrangement of moments along the c axis. Using the previous DFT results for a 3.5 K experimental cell, the $Cm'm'm$ moment arrangement is 0.62 meV/atom higher in energy than the $P_C bam$ moment arrangement [18], so, trivially, for an isolated $2.10\,\mu_B$ moment along c paired with an antialigned 5.5 T field, the energy gain for flipping the moment is 1.34 meV ($2\mu_{Co}B$). The proposed magnetic structure change is, therefore, energetically reasonable. In the ferromagnetic-dominated field region, we tracked the (110) transition with increasing temperature (Fig. S8). Up to 20 K, we do not observe a sharp drop or leveling off of the intensity but rather a nearly linear decrease in intensity. Similarly, the magnetic susceptibility at high field, even up to 7 T (Fig. S8), does not show the typical sharp rise of a paramagnetic to ferromagnetic transition, suggesting that the high-field magnetic ordering is driven by field overcoming the material's interchain antiferromagnetic exchange interactions instead of by dominant interchain ferromagnetic exchange interactions.

C. Spin model from high-field IR spectroscopy

To explore the spin dynamics of Li_2CoCl_4 under high applied fields, we collected IR spectroscopy data up to 17.5 T.
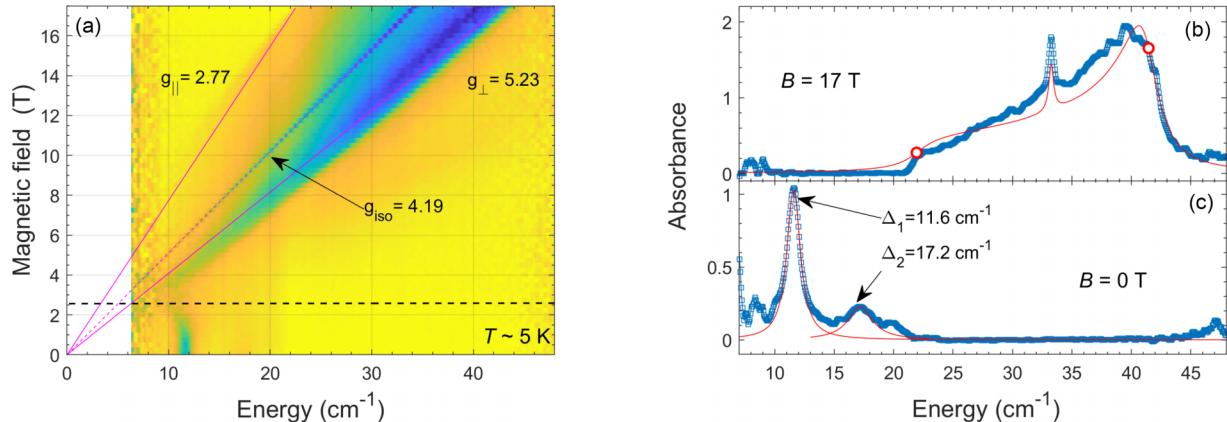
FIG. 5. (a) The magnetic resonance absorption heat map at 5 K is shown with magenta lines representing the resonance conditions for different g factors for a noninteracting spin-$\frac{1}{2}$ model. The black dashed line corresponds to the transition to the high-field magnetic phase from magnetic susceptibility data in Ref. [18] ($\sim$2.5 T at 5 K). (b) A heat map slice at 17 T (blue dots) shows agreement with a simulated powder spectrum (red line) with 98% of the intensity from a spin-$\frac{1}{2}$ site with an anisotropic g factor ($g_\perp$ and $g_\parallel$, magenta points) and 2% from a site with an isotropic g factor of 4.19. (c) Lorentzian peak fits (red curves) to a heat map slice at zero field demonstrate the nearly twofold linewidth difference in the spin-gap peaks.

At lower energies within the detection range, the normalized magnetic resonance absorption contains a broad continuum [Fig. 5(a)]. The broad continuum reveals the strongly anisotropic nature of the magnetic moment of the Co^{2+} cation in the Li_2CoCl_4 powder sample. At magnetic fields significantly above the moment saturation field, the Zeeman energy dominates the antiferromagnetic spin-spin interactions, and spin dynamics converge toward those of free-ion spin precession [30]. For many low-dimensional cobalt compounds with octahedral ligand environments, the magnetic properties are well described by an effective spin-$\frac{1}{2}$ model due to a well-separated ground state Kramers doublet [31–34]. Therefore, as a first approximation, we use a noninteracting spin-$\frac{1}{2}$ framework to extract g factors from the high-field IR data.

1. Noninteracting spin-$\frac{1}{2}$ model

In the free spin-$\frac{1}{2}$ framework, an applied magnetic field splits the $m = +\frac{1}{2}$ and $m = -\frac{1}{2}$ states (Zeeman splitting) by the energy $E = g\mu_B B$, where E can be directly observed as a peak in the absorption spectrum. The parameter g is the effective g factor, whose value depends on the orientation of the magnetic field relative to the anisotropy axis. Due to the randomly oriented grains in the polycrystalline sample, the absorption associated with the Zeeman splitting is distributed over a frequency range that broadens with magnetic field, resulting in the continuum in Fig. 5(a). The asymmetric line shape of the absorption spectrum [Fig. 5(b)] indicates a system with axial symmetry, and indeed the $CoCl_6$ octahedra in Li_2CoCl_4 are slightly compressed along the b axis [ratio of the Co-Cl bond length along b to the length within the ac plane of 0.986(2)], producing a tetragonal distortion of the octahedra. The continuum is bounded by resonance conditions $g_\parallel \mu_B B$ and $g_\perp \mu_B B$ with more intensity on the $g_\perp$ side [35], where $\parallel$ and $\perp$ are relative to the compressed $CoCl_6$ axis. Since the continuum edges at the resonance energies associated with $g_\parallel$ and $g_\perp$ are smeared by peak broadening, we simulated

the absorption spectrum using a powder-averaged line shape and varied the g factors to obtain a match [Fig. 5(b)]. The fit anisotropic g factors are $g_\parallel = 2.77$ and $g_\perp = 5.23$. The corresponding resonance lines confine the magnetic absorption spectrum for a free cobalt ion, but the experimental data diverge from the lines below $\sim$10 T, where exchange interactions produce a more complex picture of collective spin excitations [Fig. 5(a)].

Also of note is the narrow feature within the broader continuum of Fig. 5(a) at high fields. The line shape is well fit by a single peak, indicating an isotropic g factor of 4.19. The peak may originate from a Co^{2+} site with minimal axial distortion. A similar peak was observed in the X-band EPR spectrum of $LiCoO_2$ and was ascribed to a high-spin Co^{2+} site on the surface of a polycrystalline sample [36,37]. Powder spectrum simulations that consider a mixture of isotropic (surface) and anisotropic (bulk) Co^{2+} sites [Fig. 5(b)] indicate that 2% of the Co^{2+} sites are isotropic. We will regard the fraction as a small paramagnetic impurity and will ignore it while interpreting other magnetic property measurements of powder samples. The fit g factors in the noninteracting spin-$\frac{1}{2}$ model are significantly larger than the isotropic, free-electron value of $g = 2$. The discrepancy can be well explained by an effective Hamiltonian that accounts for spin-orbit coupling.

2. Effective spin-orbit coupling model

To build a spin-orbit coupling model, we first consider the ligand environment and paramagnetic susceptibility of Co^{2+} in Li_2CoCl_4. The Co^{2+} cations are octahedrally coordinated to Cl^- anions, and the magnetic susceptibility indicates that the Co^{2+} cations are high-spin with unquenched orbital angular momentum [18], i.e., significantly influenced by SOC. The anisotropic magnetism of a high-spin Co^{2+} cation in a local octahedral environment is well studied [32,38–41]. The ground state is a $^4T_{1g}(^4F)$ orbital triplet with $L_{\rm eff} = 1$ and $S = \frac{3}{2}$, and the following Hamiltonian describes the
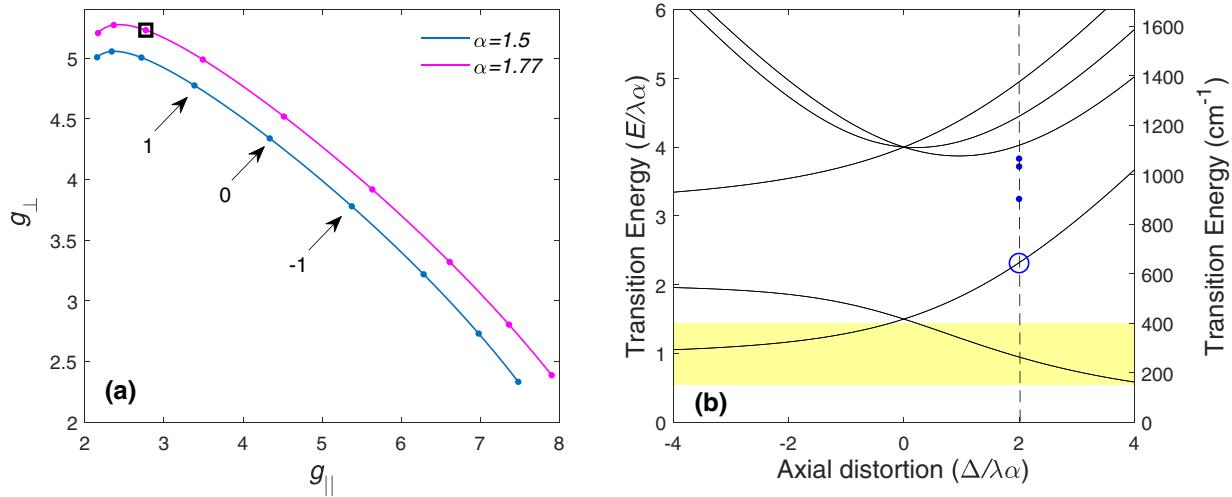
FIG. 6. (a) Curves show the change in g-factor anisotropy with axial distortion for orbital reduction factors of 1.5 and 1.77 with points indicating integer values of $\Delta/(\lambda\alpha)$. (b) The spectrum for a free Co^{2+} ion is calculated for $\alpha = 1.77$ as a function of $E/(\lambda\alpha)$ (left-hand axis) or assuming $\lambda = 157$ cm^{-1} (right-hand axis). The dashed line matches the distortion derived from the experimental g-factor anisotropy. The shaded area is opaque to FIR radiation, preventing observation of transitions to the first excited Kramers doublet.

low-energy diagram [41]:

$$H = -\lambda \mathbf{L} \cdot \alpha \cdot \mathbf{S} - \Delta\left(L_z^2 - \tfrac{2}{3}\right) + \mu_B \mathbf{B}(g_e \mathbf{S} - \alpha \mathbf{L}). \quad (1)$$

λ is the spin-orbit coupling constant, Δ is the crystal field energy due to axial distortion, $\mathbf{B}$ is the magnetic field vector, g_e is the free-electron g factor, and α is the orbital reduction factor. The orbital reduction factor quantifies the covalence of metal-ligand bonds and admixture of higher-energy orbital states, e.g., $^4T_{1g}(^4P)$. Without axial distortion or a magnetic field, the first-order spin-orbit coupling splits the 12-fold degenerate $^4T_{1g}$ state, making a $J = \frac{1}{2}$ doublet the lowest energy level. The doublet is separated by $9\lambda/4$ from the first excited quartet state (49.7 meV assuming a free-ion spin-orbit coupling constant of 178 cm^{-1}) [38,40,42]. The well-separated, ground-state doublet, therefore, produces effective spin-$\frac{1}{2}$ behavior at low temperatures with an isotropic g factor of $g_0 = (10 + 2\alpha)/3$ with α values ranging from 1 (strong crystal field) to 1.5 (weak crystal field), resulting in isotropic g factors between 4 and 4.33 [43].

Next, axial distortion should be considered because of the aforementioned tetragonal distortion of the CoCl$_6$ octahedra in Li$_2$CoCl$_4$. Axial distortion of the ideal octahedral environment of the Co^{2+} ion further splits the J manifold into six Kramers doublets and leads to anisotropy of the g factor. For distortion values (Δ) small relative to the spin-orbit exchange constant ($\lambda\alpha$), the g-factor anisotropy is approximately [43]

$$g_\perp = g_0 + \frac{8\Delta}{27\lambda\alpha}(\alpha + 2),$$
$$g_\parallel = g_0 - 2\frac{8\Delta}{27\lambda\alpha}(\alpha + 2). \quad (2)$$

The average g factor in this case remains independent of the distortion effects since $g_{avg} = (2g_\perp + g_\parallel)/3 = g_0$. Using the fit spectroscopic g factors $g_\parallel = 2.77$ and $g_\perp = 5.23$, we can calculate a g_{avg} of 4.41, which agrees well with the predicted isotropic g factor of 4.33 for high-spin Co^{2+} ion in the weak crystal field limit. The calculated g_{avg} also corroborates the

neutron diffraction moment, which we would expect to equal $g_{avg}J\mu_B = 2.2\mu_B$ if $J = \frac{1}{2}$. Therefore, the observed g factors for Li$_2$CoCl$_4$ confirm a $J = \frac{1}{2}$ (Kramers doublet) ground state.

Having confirmed the applicability of the spin-orbit coupling model, we can solve the Hamiltonian [Eq. (1)] to further probe the interplay between the spin-orbit exchange constant and crystal field axial distortion in Li$_2$CoCl$_4$. Using the EASYSPIN package [28], we tuned the ratio of the axial distortion to the spin-orbit exchange constant, $\Delta/(\lambda\alpha)$, and calculated the resulting changes in $g_\parallel$ and $g_\perp$ [Fig. 6(a)]. The experimental g-factor values are well described by a $\Delta/(\lambda\alpha)$ ratio of 2 and a reduction factor (α) of 1.77, which is close to the weak crystal field case of 1.5. The relatively small $\Delta/(\lambda\alpha)$ ratio [38] is indicative of a system where spin-orbit coupling plays a significant role [41]. The reduction factor is reasonably similar to that of other cobalt salts [38], though the value is outside the expected limits of [1,1.5] for a noninteracting system, highlighting a deficiency of neglecting the magnetic coupling between neighboring Co^{2+} ions [43].

3. Observed excitations predicted by the SOC model

To assess the SOC model at higher energies in the absorption spectrum, we calculated the energy difference between the ground-state and higher-energy Kramers doublets as a function of the $\Delta/(\lambda\alpha)$ ratio [Fig. 6(b)] to compare with the experimental data. Since an applied magnetic field further splits the Kramers doublets, we can distinguish spectroscopic peaks associated with the transitions from other spectroscopic features in the experimental spectrum. For example, a pronounced peak at 644 cm^{-1} shifts and broadens under an applied magnetic field (Fig. 7). Assuming $\Delta/(\lambda\alpha) = 2$, we attribute this energy to a transition from the ground state to the second excited Kramers doublet, denoted by a blue circle in Fig. 6(b). Using the previously estimated value of α (1.77), this energy yields a spin-orbit coupling constant of $\lambda = 157$ cm^{-1}, consistent with the 178 cm^{-1} value for a free Co^{2+} ion [38]. The transition to the first excited state, however, is
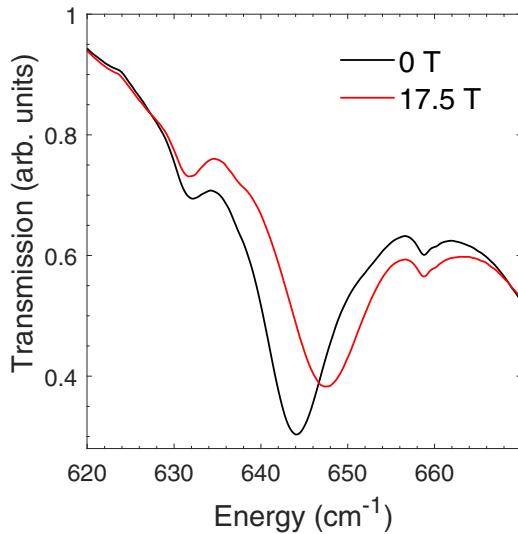
FIG. 7. The transmission spectra of the Li_2CoCl_4 powder sample measured at 0 and 17.5 T. The peak at 644 cm^{-1} shifts under high magnetic fields, while the small peaks, likely associated with phonons, remain at the same position.

not observed in the spectrum because of a strong absorption band between 200 and 400 cm^{-1}. Nevertheless, additional field-dependent spectral features [blue dots in Fig. 6(b)] were observed at higher energies (Fig. S9 [29]) and are likely associated with the remaining inter-Kramers doublet transitions. The model, therefore, qualitatively captures the anisotropic physics of Co^{2+} in Li_2CoCl_4 at higher energies in the measured absorption spectrum.

4. Paramagnetic magnetization and magnetic susceptibility

In addition to predicting IR excitations, the SOC model can be compared to experimental magnetization and magnetic susceptibility data, where the contributions from low-lying excited states are relevant. Figure 8 compares the experimental data in the paramagnetic region to EASYSPIN calculations utilizing Eq. (1) for three cases: a noninteracting spin-$\frac{1}{2}$ model with the g factors from our high-field spectroscopy data; a spin-orbit coupling model with the α, Δ, and λ parameters fit to our high-field spectroscopy data; and a spin-orbit coupling model with spectroscopic parameters optimized to fit the experimental magnetization and magnetic susceptibility. All three models qualitatively match the shape of the magnetization data and indicate a saturated moment near 2–2.75 μ_B, but they differ significantly in describing the susceptibility data. While both spin-orbit coupling models reasonably match the low- and high-temperature slopes of the susceptibility, the spin-$\frac{1}{2}$ model only captures the low-temperature behavior. Improvements to the spin-orbit coupling model would need to consider higher-order spin-orbit interactions and electronic structure effects.

5. Spin gaps below the saturation field

The approximation of free spin dynamics in high magnetic fields, of course, breaks down at lower magnetic fields where the spin-spin interactions are dominant in determining the excitation spectrum. At zero field, we observe a strong peak at 11.6 cm^{-1} and a weaker satellite at 17.2 cm^{-1} [Fig. 5(c)] that we attribute to spin gaps in the collective spin excitations of Li_2CoCl_4. Within a free-ion framework, the observed 11.6 cm^{-1} gap could be interpreted as the zero-field energy of a $S = \frac{3}{2}$ system. Exploring this possibility, we found moderate agreement between the experimental data and a $S = \frac{3}{2}$ Hamiltonian with a single-ion anisotropy of $D = 5.8$ cm^{-1} and anisotropic g factors of $g_\perp = 4.50$ and $g_\parallel = 4.16$ (Fig. S10 [29]). However, to observe a first excited Kramers doublet ~ 10 cm^{-1} would require extremely high axial distortions [Fig. 6(b)], which would be inconsistent with the model's g factors [Fig. 6(a)].
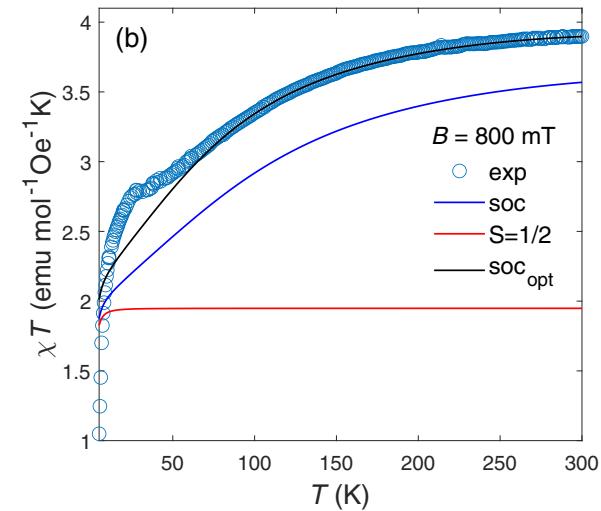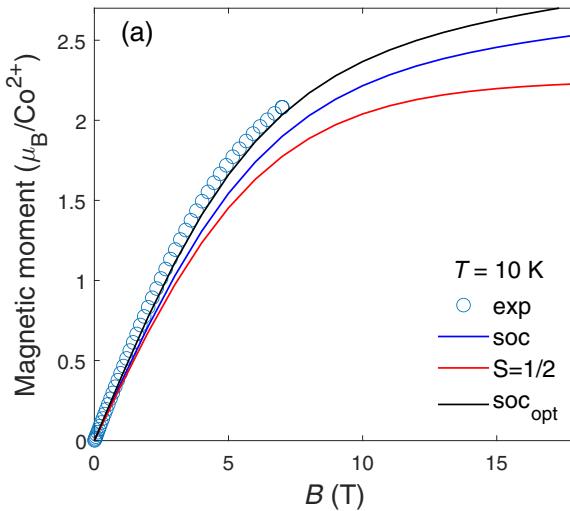
FIG. 8. Experimental (a) magnetization data at 10 K and (b) susceptibility data at 0.8 T on Li_2CoCl_4 powder (exp) are presented for a spin-$\frac{1}{2}$ model using $g_\perp = 5.23$ and $g_\parallel = 2.77$ ($S = 1/2$); a spin-orbit coupling model using the spectroscopically determined parameters $\alpha = 1.77$, $\Delta/(\lambda\alpha) = 2$, and $\lambda = 157$ cm^{-1} (soc); and a spin-orbit coupling model using the parameters $\alpha = 2$, $\Delta/(\lambda\alpha) = 2.2$, and $\lambda = 110$ cm^{-1}, adjusted to match the experimental data (soc$_{opt}$).

The $11.6\,\mathrm{cm}^{-1}$ and $17.2\,\mathrm{cm}^{-1}$ spin gaps also cannot be explained using the phenomenological theory of antiferromagnetic resonance (AFMR) for collinear magnets with two-axis magnetic anisotropy [44]. The model predicts two excitation modes attributed to spin-flop and spin-flip reorientations with increasing magnetic field. The magnetic field softens the AFMR resonance energies until the spin gaps close at the critical fields, which are directly related to the zero-field energies by the g factor. But for a spin-flop field of 1.6 T (B_{sf}) and a resonance frequency (ω) of $11.6\,\mathrm{cm}^{-1}$, the necessary g factor would be $g = \omega/(\mu_{\mathrm{B}}B_{\mathrm{sf}}) = 15.5$, significantly above our observed g factors. For the features to be AFMR modes, the zero-field gap would have to be much smaller or the spin-flop field much larger. Therefore, understanding the low-field spectroscopic data requires a more detailed microscopic model involving anisotropic spin-spin exchange interactions.

D. Evidence of XY-like anisotropy

A notable implication of our IR spectroscopy data is XY-like magnetism of the Co^{2+} cation in Li_2CoCl_4 since $g_\perp > g_\parallel$. Transition energies calculated with the SOC model [Fig. 6(b)] predict an energy gap between the two lowest doublets of $264\,\mathrm{cm}^{-1}$ (32.7 meV), indicating that Co^{2+} ions' behavior in Li_2CoCl_4 is dominated by the ground-state Kramers doublet at low temperatures. This state can be mapped to an effective spin-$\frac{1}{2}$ state with an exchange interaction, JS_1S_2, between next-neighbor spins exhibiting anisotropy of the type $\beta = J_z/J_x \neq 1$. Solving the spin-orbit Hamiltonian [Eq. (1)] using spectroscopically determined parameters enables an estimation of the magnetic coupling anisotropy, yielding $\beta = 0.41$ for Li_2CoCl_4 (see the Supplemental Material for details [29] and Refs. [19,31,32,38] therein). This value of β classifies Li_2CoCl_4 as a system with easy-plane anisotropy, consistent with $g_\perp > g_\parallel$. Most Co-based chain materials with octahedral CoX_6 coordination, such as $CsCoCl_3$ [19], $CoCl_2 \cdot 2H_2O$ [45], $CoNb_2O_6$ [33], $[Co(NCS)_2(4 - \mathrm{methoxypyridine})_2]_n$ [46], $Co(N_2H_5)_2(SO_4)_2$ [47], and $(Ba, Sr)Co_2V_2O_8$ [34], exhibit Ising anisotropy ($\beta > 1$). The tetragonal distortion of the $CoCl_6$ octahedron in Li_2CoCl_4, in contrast to the trigonal distortion in those systems, may serve as the underlying mechanism for XY anisotropy.

The neutron diffraction data are also compatible with, though not definitive regarding, easy-(ac-)plane anisotropy. The data suggest a preference for moment alignment along the c axis, but there were no observed reflections that violate a rotation through the a axis during the spin reorientation, and the refinement with moment components along a and c ($C2'/m'$ space group) was nearly identical to that with moments only along c. In contrast, the zero-field structure has no moment component along b, and under an applied field the maximal magnetic space group with moments solely along b was incompatible with the magnetic intensity. These features of the neutron data suggest that the c axis or ac plane may be the material's easy axis/plane, which is consistent with the IR data. If the system has easy-axis anisotropy along c instead of easy-plane anisotropy, this is still compatible with the XY-anisotropy description, which neglects spin-spin exchange interactions that would, presumably, distinguish the a and c axes. The SOC model was also overparameterized

if we introduced additional anisotropy to try to distinguish a and c, leaving XY anisotropy as the best description with the available data.

Qualitatively, the magnetic heat capacity of Li_2CoCl_4 at temperatures just above the long-range magnetic ordering [18] displays a hump similar to that of the predicted heat capacity for an isolated spin-$\frac{1}{2}$, XY chain with $J_x = J_y$, $J_z = 0$, and an applied field along the z direction [48]. Fitting the heat capacity of Cs_2CoCl_4 [49], a compound with tetrahedrally coordinated Co^{2+} which also has a long-range ordering lambda peak and a hump in its magnetic heat capacity, to this model gives an intrachain exchange interaction parameter. However, we could not similarly fit the heat capacity of polycrystalline Li_2CoCl_4, which has appreciable interchain interactions. The hump is, therefore, better understood as stemming from short-range order due to the spatially distributed spin reorientation with increasing field.

IV. CONCLUSIONS

Overall, Li_2CoCl_4 exhibits strongly anisotropic magnetic properties. At zero field, neutron diffraction shows that the moments within chains of octahedrally coordinated Co^{2+} align ferromagnetically while aligning antiferromagnetically between nearest-neighboring chains. At nonzero fields below 1.6 T, neutron diffraction shows that the antiferromagnetic structure is unchanged, but with increasing magnetic field, the antialigned chains undergo a spin reorientation to a ferromagnetic state, likely with a preference for moment alignment along the c axis. Based on refinements including the antiferromagnetic P_Cbam phase and a $Cm'm'm$ ferromagnetic phase, a majority of the sample becomes ferromagnetic near 3.5 T. The chains do not transition to a ferrimagnetic state at intermediate fields as in $CoCl_2 \cdot 2H_2O$.

The high-field FIR data are well described by a spin-orbit coupling model that confirms a well-separated Kramers doublet ground state ($J = \frac{1}{2}$) for the Co^{2+} ion that is approximately 32.7 meV below the first excited state. The $J = \frac{1}{2}$ ground state and strong spin-orbit coupling explain the qualitative shape of magnetization and susceptibility data in the paramagnetic region, as well as the refined magnetic moment from neutron diffraction, the entropy recovery extracted from previous heat capacity data, and the difficulty in fitting the paramagnetic susceptibility to a purely Curie-Weiss shape. Still, the two spin gaps at 11.6 and $17.2\,\mathrm{cm}^{-1}$ in the zero-field spectrum highlight the need for a model that also accounts for the anisotropy of spin-spin interactions. The tetragonal distortion of the $CoCl_6$ octahedra may also promote XY-like magnetic interactions, with an estimated interaction parameter ratio J_z/J_x of 0.41. XY anisotropy distinguishes Li_2CoCl_4 from other Co^{2+} chain magnets that have trigonally distorted octahedra and display Ising-like anisotropy.

Further work should explore this anisotropy and its influence on the unexplained spin gaps below the moment saturation field by developing a model of spin-spin interactions between the cobalt ions. The models will be aided by single crystal neutron scattering experiments. Single crystal magnetization and neutron data along the three crystallographic axes would also improve the description of the magnetic behavior, allowing for a more precise determination

of the moment saturation field and a definitive description of the spin reorientation at intermediate magnetic fields. Li_2CoCl_4, therefore, offers a rare opportunity to study the combined effects of effective spin-$\frac{1}{2}$ behavior and XY-like magnetic anisotropy on spin dynamics in an octahedrally coordinated Co^{2+} system.

ACKNOWLEDGMENTS

DATA AVAILABILITY

The data that support the findings of this article are not publicly available upon publication because it is not technically feasible and/or the cost of preparing, depositing, and hosting the data would be prohibitive within the terms of this research project. The data are available from the authors upon reasonable request.

[1] A. Vasiliev, O. Volkova, E. Zvereva, and M. Markina, Milestones of low-D quantum magnetism, npj Quantum Mater. **3**, 18 (2018).

[2] R. Coldea, D. A. Tennant, E. M. Wheeler, E. Wawrzynska, D. Prabhakaran, M. Telling, K. Habicht, P. Smeibidl, and K. Kiefer, Quantum criticality in an Ising chain: Experimental evidence for emergent E_8 symmetry, Science **327**, 177 (2010).

[3] J. Larsen, T. K. Schäffer, U. B. Hansen, S. L. Holm, S. R. Ahl, R. Toft-Petersen, J. Taylor, G. Ehlers, J. Jensen, H. M. Rønnow, K. Lefmann, and N. B. Christensen, Spin excitations and quantum criticality in the quasi-one-dimensional Ising-like ferromagnet $CoCl_2 \cdot 2D_2O$ in a transverse field, Phys. Rev. B **96**, 174424 (2017).

[4] Z. Wang, T. Lorenz, D. I. Gorbunov, P. T. Cong, Y. Kohama, S. Niesen, O. Breunig, J. Engelmayer, A. Herman, J. Wu *et al.*, Quantum criticality of an Ising-like spin-$\frac{1}{2}$ antiferromagnetic chain in a transverse magnetic field, Phys. Rev. Lett. **120**, 207205 (2018).

[5] M. H. Karigerasi, L. K. Wagner, and D. P. Shoemaker, Uncovering anisotropic magnetic phases via fast dimensionality analysis, Phys. Rev. Mater. **2**, 094403 (2018).

[6] R. Kanno, Y. Takeda, and O. Yamamoto, Ionic conductivity of solid lithium ion conductors with the spinel structure: Li_2MCl_4 (M = Mg, Mn, Fe, Cd), Mater. Res. Bull. **16**, 999 (1981).

[7] R. Kanno, Y. Takeda, K. Takada, and O. Yamamoto, Phase diagram and ionic conductivity of the lithium chloride-iron (II) chloride system, Solid State Ion. **9-10**, 153 (1983).

[8] W. Schmidt and H. D. Lutz, Fast ionic conductivity and dielectric properties of the lithium halide spinels Li_2MnCl_4, Li_2CdCl_4, Li_2MnBr_4, and Li_2CdBr_4, Ber. Bunsengesellschaft Phys. Chem. **88**, 720 (1984).

[9] R. Kanno, Y. Takeda, A. Takahashi, O. Yamamoto, R. Suyama, and S. Kume, New double chloride in the $LiCl$-$CoCl_2$ system: II. Preparation, crystal structure, phase transformation, and ionic conductivity of Li_2CoCl_4 spinel, J. Solid State Chem. **71**, 196 (1987).

[10] R. Kanno, Y. Takeda, and O. Yamamoto, Structure, ionic conductivity and phase transformation of double chloride spinels, Solid State Ion. **28–30**, 1276 (1988).

[11] R. Kanno, Y. Takeda, A. Takahashi, O. Yamamoto, R. Suyama, and S. Kume, Structure, ionic conductivity, and phase transformation in new polymorphs of the double chloride spinel, Li_2FeCl_4, J. Solid State Chem. **72**, 363 (1988).

[12] R. Kanno, Y. Takeda, A. Matsumoto, O. Yamamoto, R. Suyama, and S. Kume, Synthesis, structure, ionic conductivity, and phase transformation of new double chloride spinel, Li_2CrCl_4, J. Solid State Chem. **75**, 41 (1988).

[13] H. D. Lutz, P. Kuske, and K. Wussow, Ionic motion of tetrahedrally and octahedrally coordinated lithium ions in ternary and quaternary halides, Solid State Ion. **28–30**, 1282 (1988).

[14] K. Wussow, H. Haeuseler, P. Kuske, W. Schmidt, and H. D. Lutz, Lattice vibration spectra: XLVIII. Infrared and Raman studies of spinel-type fast Ionic conductors Li_2MCl_4 (M = Mg, V, Cr, Mn, Fe, Co, Zn, Cd) and Li_2MnBr_4, J. Solid State Chem. **78**, 117 (1989).

[15] H. D. Lutz, Fast lithium-ion conductors - chemistry and application, Nachr. Chem. Tech. Lab. **43**, 418 (1995).

[16] R. Kanno, Y. Takeda, K. Takada, and O. Yamamoto, Ionic conductivity and phase transition of the spinel system $Li_{2-2x}M_{1+x}Cl_4$ (M = Mg, Mn, Cd), J. Electrochem. Soc. **131**, 469 (1984).

[17] J. Cerisier, C. Guillot, P. Palvadeau, and M. Spiesser, Ionic conductors $Li_{1+x}FeCl_4$ part 1: Preparation and characterization, Mater. Res. Bull. **21**, 575 (1986).

[18] Z. W. Riedel, Z. Jiang, M. Avdeev, A. Schleife, and D. P. Shoemaker, Zero-field magnetic structure and metamagnetic phase transitions of the cobalt chain compound Li_2CoCl_4, Phys. Rev. Mater. **7**, 104405 (2023).

[19] N. Achiwa, Linear antiferromagnetic chains in hexagonal $ABCl_3$-type compounds (A; Cs, or Rb, B; Cu, Ni, Co, or Fe), J. Phys. Soc. Jpn. **27**, 561 (1969).

[20] J. K. Kjems, J. Als-Nielsen, and H. Fogedby, Spin-wave dispersion in $CoCl_2 \cdot 2D_2O$: A system of weakly coupled Ising chains, Phys. Rev. B **12**, 5190 (1975).

[21] W. Montfrooij, G. E. Granroth, D. G. Mandrus, and S. E. Nagler, Spin dynamics of the quasi-one-dimensional ferromagnet $CoCl_2 \cdot 2D_2O$, Phys. Rev. B **64**, 134426 (2001).

[22] M. Mena, N. Hänni, S. Ward, E. Hirtenlechner, R. Bewley, C. Hubig, U. Schollwöck, B. Normand, K. W. Krämer, D. F. McMorrow, and C. Rüegg, Thermal control of spin excitations in the coupled Ising-chain material $RbCoCl_3$, Phys. Rev. Lett. **124**, 257201 (2020).

[23] D. E. Cox, G. Shirane, B. C. Frazer, and A. Narath, Neutron diffraction determination of the intermediate-field magnetic structure of $CoCl_2 \cdot 2H_2O$, J. Appl. Phys. **37**, 1126 (1966).

[24] H. Weitzel and W. Schneider, Neutron diffraction determination of the magnetic phases of $CoCl_2 \cdot 2H_2O$, Solid State Commun. **14**, 1025 (1974).

[25] B. H. Toby and R. B. Von Dreele, *GSAS − II*: The genesis of a modern open-source all purpose crystallography software package, J. Appl. Crystallogr. **46**, 544 (2013).

[26] J. M. Perez-Mato, S. V. Gallego, E. S. Tasci, L. Elcoro, G. de la Flor, and M. I. Aroyo, Symmetry-based computational tools for magnetic crystallography, Annu. Rev. Mater. Res. **45**, 217 (2015).

[27] K. Momma and F. Izumi, *V ESTA* 3 for three-dimensional visualization of crystal, volumetric and morphology data, J. Appl. Crystallogr. **44**, 1272 (2011).

[28] S. Stoll and A. Schweiger, EasySpin, a comprehensive software package for spectral simulation and analysis in EPR, J. Magn. Reson. **178**, 42 (2006).

[29] See Supplemental Material at https://link.aps.org/supplemental/10.1103/tqwb-v5r2 for additional information, which includes Ref. [31].

[30] T. Nagamiya, K. Yosida, and R. Kubo, Antiferromagnetism, Adv. Phys. **4**, 1 (1955).

[31] T. Oguchi, Theory of magnetism in $CoCl_2 \cdot 2H_2O$, J. Phys. Soc. Jpn. **20**, 2236 (1965).

[32] H. Shiba, Y. Ueda, K. Okunishi, S. Kimura, and K. Kindo, Exchange interaction via crystal-field excited states and its importance in $CsCoCl_3$, J. Phys. Soc. Jpn. **72**, 2326 (2003).

[33] K. Amelin, J. Engelmayer, J. Viirok, U. Nagel, T. Rõõm, T. Lorenz, and Z. Wang, Experimental observation of quantum many-body excitations of E_8 symmetry in the Ising chain ferromagnet $CoNb_2O_6$, Phys. Rev. B **102**, 104431 (2020).

[34] J. Yang, X. Wang, and J. Wu, Magnetic excitations in the one-dimensional Heisenberg-Ising model with external fields and their experimental realizations, J. Phys. A: Math. Theor. **56**, 013001 (2023).

[35] J. A. Weil and J. R. Bolton, *Electron Paramagnetic Resonance: Elementary Theory and Practical Applications* (Wiley-Interscience, Hoboken, NJ, 2007), pp. 99–105.

[36] B. Hu, F. Geng, M. Shen, C. Zhao, Q. Qiu, Y. Lin, C. Chen, W. Wen, S. Zheng, X. Hu *et al.*, A multifunctional manipulation to stabilize oxygen redox and phase transition in 4.6 V high-voltage $LiCoO_2$ with sXAS and EPR studies, J. Power Sources **516**, 230661 (2021).

[37] B. Hu, F. Geng, M. Shen, and B. Hu, The study of electrochemical cycle for $LiCoO_2$ by dual-mode EPR, Magn. Reson. Lett. **3**, 61 (2023).

[38] A. Abragam and M. H. L. Pryce, The theory of paramagnetic resonance in hydrated cobalt salts, Proc. R. Soc. Lond. A **206**, 173 (1951).

[39] M. E. Lines, Magnetic properties of $CoCl_2$ and $NiCl_2$, Phys. Rev. **131**, 546 (1963).

[40] F. E. Mabbs and D. J. Machin, *Magnetism and Transition Metal Complexes* (Chapman and Hall, London, 1973).

[41] O. Kahn, *Molecular Magnetism* (Wiley-VCH, Weinheim, 1993).

[42] J. B. Goodenough, Spin-orbit-coupling effects in transition-metal compounds, Phys. Rev. **171**, 466 (1968).

[43] F. Lloret, M. Julve, J. Cano, R. Ruiz-García, and E. Pardo, Magnetic properties of six-coordinated high-spin cobalt (II) complexes: Theoretical background and its application, Inorg. Chim. Acta **361**, 3432 (2008).

[44] V. N. Glazkov, A. I. Smirnov, A. Revcolevschi, and G. Dhalenne, Magnetic resonance study of the spin-reorientation transitions in the quasi-one-dimensional antiferromagnet $BaCu_2Si_2O_7$, Phys. Rev. B **72**, 104401 (2005).

[45] U. Hansen, O. F. Syljuasen, J. Jensen, T. Schaffer, C. Andersen, M. Boehm, J. A. Rodriguez-Rivera, N. B. Christensen, and K. Lefmann, Magnetic Bloch oscillations and domain wall dynamics in a near-Ising ferromagnetic chain, Nat. Commun. **13**, 2547 (2022).

[46] M. Rams, A. Jochim, M. Böhme, T. Lohmiller, M. Ceglarska, M. M. Rams, A. Schnegg, W. Plass, and C. Näther, Single-chain magnet based on cobalt (II) thiocyanate as XXZ spin chain, Chem. A Eur. J. **26**, 2837 (2020).

[47] S. Calder, L. D. Sanjeewa, V. O. Garlea, J. Xing, R. J. Terry, and J. W. Kolis, Magnetic interactions in the one-dimensional spin-chain metal-organic compounds $M(N_2H_5)_2(SO_4)_2$ ($M =$ Cu, Co, Mn), Phys. Rev. Mater. **6**, 124407 (2022).

[48] S. Katsura, Statistical mechanics of the anisotropic linear Heisenberg model, Phys. Rev. **127**, 1508 (1962).

[49] H. A. Algra, L. J. De Jongh, H. W. J. Blöte, W. J. Huiskamp, and R. L. Carlin, Heat capacity of Cs_2CoCl_4 below 1 K, compared with the S = $\frac{1}{2}$ linear chain *XY* model, Physica B+C **82**, 239 (1976).